Joule

CellPress

Article

Nanoscale Mapping of Extrinsic Interfaces in Hybrid Solid Electrolytes

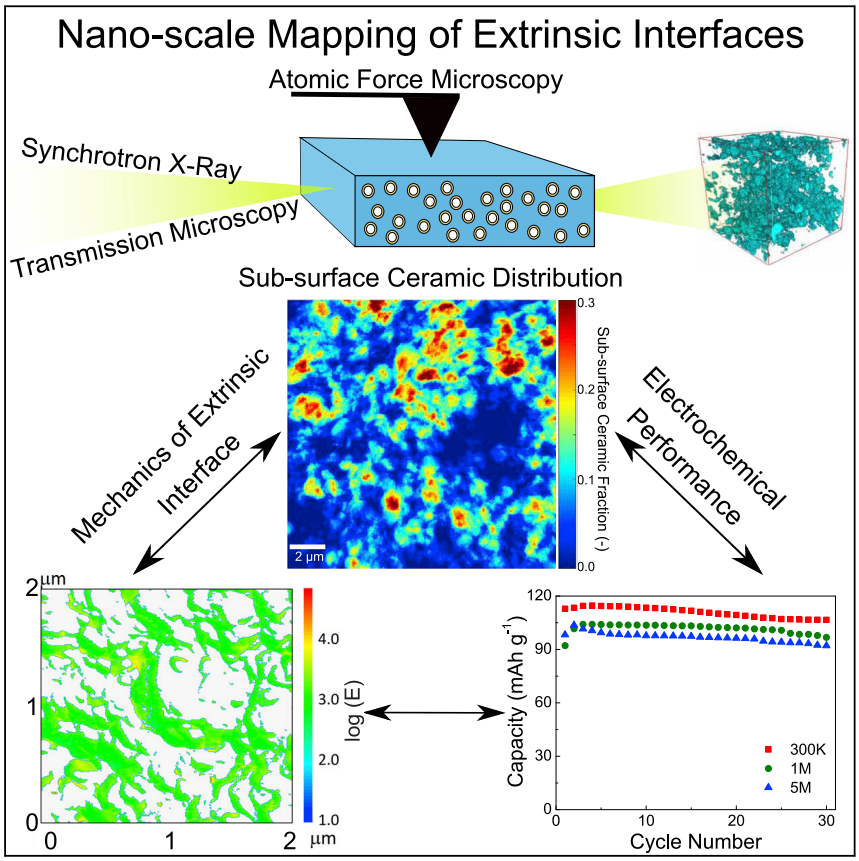

Interfaces between a solid electrolyte and electrodes in ASSBs need to be carefully engineered to enable high performance. This study leverages advanced characterization techniques (atomic force microscopy and synchrotron X-ray transmission microscopy) as well as computational tools to understand the mechanical response of electrode|electrolyte interfaces in model hybrid electrolyte systems. The impact of mechanical properties of the extrinsic interfaces on electrochemical performance is evaluated. Active control of interfacial properties is identified as a potential route to engineer high-performance solid-state batteries.

Marm B. Dixit, Wahid Zaman, Nicholas Hortance, ..., X. Chelsea Chen, Nina Balke, Kelsey B. Hatzell

kelsey.b.hatzell@vanderbilt.edu

HIGHLIGHTS

Mechanical properties of extrinsic interfaces mapped for model system using AFM

Sub-surface ceramic distribution correlated to variation in surface mechanics

Electrochemical performance linked to improved adhesion at extrinsic interface

Tailoring interfacial properties will enable high-performance ASSBs

Dixit et al., Joule 4, 207–221
January 15, 2020 © 2019 Elsevier Inc.
https://doi.org/10.1016/j.joule.2019.11.015

Joule

CellPress

Article

Nanoscale Mapping of Extrinsic Interfaces in Hybrid Solid Electrolytes

Marm B. Dixit,[1] Wahid Zaman,[1] Nicholas Hortance,[2] Stella Vujic,[2] Brice Harkey,[2] Fengyu Shen,[1] Wan-Yu Tsai,[3] Vincent De Andrade,[4] X. Chelsea Chen,[5] Nina Balke,[3] and Kelsey B. Hatzell[1,2,6,7,*]

SUMMARY

Inorganic-organic hybrid solid electrolytes are promising material systems for all solid-state batteries (ASSBs). These electrolytes contain numerous solid-|solid interfaces that govern transport pathways, electrode|electrolyte compatibility, and durability. This paper evaluates the role that electrode|electrolyte interfaces and electrolyte structure have on electrochemical performance. Atomic force microscopy techniques reveal how mechanical, adhesion, and morphological properties transform in a series of model hybrid solid electrolytes. These measurements are mapped to sub-surface microstructural features using synchrotron nano-tomography. Hybrid solid electrolytes with shorter polymer chains demonstrate a higher adhesion (>100 nN), Young's Modulus (6.4 GPa), capacity (114.6 mAh/g), and capacity retention (92.9%) than hybrid electrolytes with longer polymer chains (i.e., higher molecular weight). Extrinsic interfacial properties largely dictate electrochemical performance in ASSBs. Microstructural control over inorganic constituents may provide a means for tailoring interfacial properties in hybrid solid electrolytes.

INTRODUCTION

Hybrid solid electrolytes are an emerging family of solid electrolytes that are promising alternatives to liquid electrolytes for energy and power dense solid-state batteries.[1,2] These electrolytes contain an inorganic (ceramic and/or glass) ion conductor encapsulated in a polymer (organic). The inorganic ion conductor can decrease the polymer crystallinity and is also an ion conductor.[3–5] Inorganic ion conductors are typically thick (>500 μm) and hard to manufacture at scale but have excellent transport properties (conductivity and transference number)[6–8] (Figure 1A). In contrast, polymer ion conductors are easy to manufacture (<50 μm) and are more chemically stable in air than most inorganic materials. However, polymer electrolytes have lower transference numbers and ionic conductivities. Hybrid solid electrolytes aim to combine the advantages of both types of solid ion conductors for scalable applications of solid-state batteries (Figure 1A).

All solid electrolytes consist of both intrinsic interfaces formed by grains, vacancies, and material junctions and extrinsic interfaces formed at solid|solid interfaces. Intrinsic interfaces in hybrid electrolytes are largely responsible for the ion conduction pathways[9] (Figure 1B). The contact region between the polymer and inorganic media is an example of an intrinsic interface. The confined interfacial polymer region demonstrates different transport properties than the bulk polymer and may augment transport properties because of Lewis acid interactions between the mobile ion and surface functional groups[10] The ability to tune ion conduction pathways within the electrolyte may provide a means to ameliorate dendrite formation and control plating mechanisms. There are

Context & Scale

ASSBs are promising high-energy density energy storage devices. Hybrid electrolytes are material systems containing an organic and inorganic ion conductor that can achieve manufacturing, transport, and mechanical requirements of ASSBs. Hybrid electrolytes contain material junctions between the organic and inorganic phases (intrinsic) and between the electrode and electrolyte (extrinsic). Both extrinsic and intrinsic interfaces in these systems witness dynamic physical and chemical changes that can adversely impact the battery performance. Limited experimental knowledge is available for these interfaces due to the relative difficulty of accessing these interfaces. Rational design of interfaces is crucial to achieve stable, high-performance ASSBs. This work evaluates extrinsic interfaces for a model PEO-LLZO hybrid electrolyte system and shows the impact of interfacial properties on electrochemical performance.

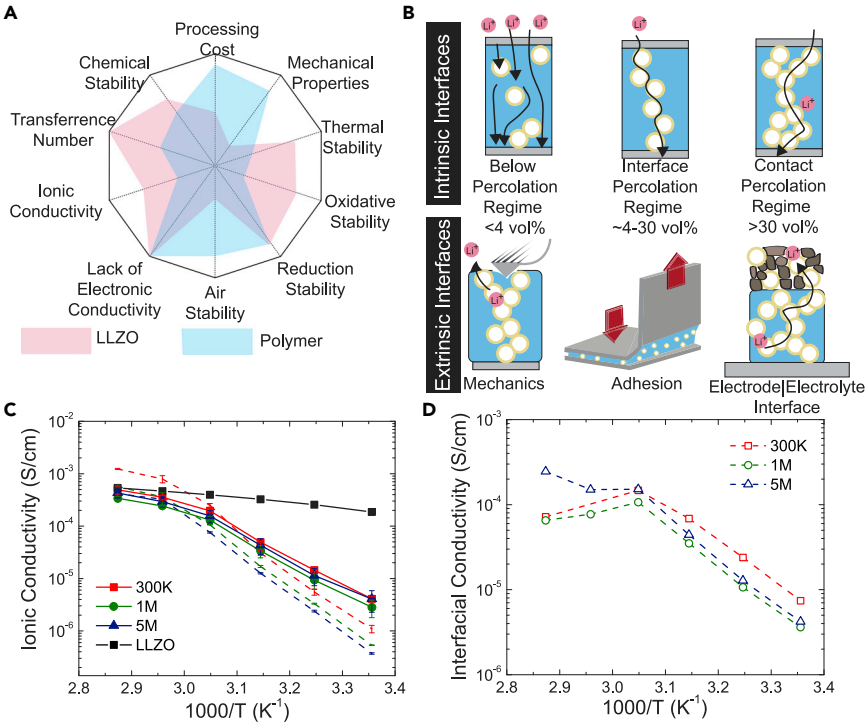

Figure 1. Summary of Solid Electrolytes and Ion Transport Properties of Hybrid Electrolytes

(A) Radar plot of salient features of ceramic and polymer solid electrolytes required to achieve high-performance ASSBs. Hybrid polymer electrolytes can overcome shortcomings of individual material types. Note that the radar plot assesses the strengths and weaknesses of individual material types qualitatively.

(B) Schematic showing the two kinds of interfaces present in hybrid electrolyte systems: intrinsic interfaces and extrinsic interfaces, their characteristics and impact.

(C) Ionic conductivities of HPEs (solid lines) and polymer electrolytes (dashed lines).

(D) Interface conductivities with 300 K, 1 M, and 5 M PEO as estimated using the effective mean field theory model (see Figure S3).

two percolation thresholds that exist in hybrid electrolytes: (1) long-range connectivity of inorganic particles (contact mode) (Figure 1B) and (2) long-range connectivity of the confined polymer region. The former is achieved at high loadings of 33 vol % (ceramic:polymer) and the latter is achieved at ≈4 vol % (ceramic:polymer). The literature is filled with contradicting observations supporting optimum transport through high-ceramic loading hybrid electrolytes[11–14] and low-ceramic loading electrolytes (interface percolated).[15–18] There is currently a knowledge gap regarding transport mechanisms in these hybrid solid electrolyte systems.

Extrinsic interfaces that emerge during device integration (i.e., electrode-|electrolyte) are responsible for ion transport between an ion conducting phase (electrolyte) and a mixed ion and electron conducting phase (i.e., electrode). The nature of ionic transport at intrinsic and extrinsic interfaces is important for mitigating chemical and structural instabilities. Extrinsic interface instabilities are responsible for high interfacial resistances. This interfacial resistance can grow and ultimately cause a decrease in capacity or catastrophic failure because of dendrite formation,[19–22] capacity loss via the formation of dead Li,[23] regions of excess and deficient Li content,[24,25] and interface delamination.[9,18,26,27] Currently, there are very few reports that describe the role extrinsic interfaces play on cathode performance. Engineering these interfaces to promote ion transport between an ion conductor

[1]Department of Mechanical Engineering, Vanderbilt University, Nashville, TN 37240, USA

[2]Interdisciplinary Material Science Program, Vanderbilt University, Nashville, TN 37240, USA

[3]Center for Nanophase Materials Science, Oak Ridge National Laboratory, Oak Ridge, TN 37830, USA

[4]X-Ray Science Division, Argonne National Laboratory, 9700 South Cass Avenue, Lemont, IL 60439, USA

[5]Chemical Sciences Division, Oak Ridge National Laboratory, Oak Ridge, TN 37830, USA

[6]Chemical and Biomolecular Engineering, Vanderbilt University, Nashville, TN 37240, USA

[7]Lead Contact

*Correspondence: kelsey.b.hatzell@vanderbilt.edu

https://doi.org/10.1016/j.joule.2019.11.015

(electrolyte) and a mixed ion and electron conductor (electrode) presents a crucial challenge toward realizing state batteries (ASSBs).[28]

The physical properties of extrinsic interfaces (electrolyte|electrode) in hybrid electrolytes are largely unknown (Figure 1B). Lithiation and delithiation during battery cycling leads to volumetric expansion and contraction dynamics at the cathode.[29] The extrinsic interface's Young's modulus is a useful property that describes how well an electrolyte can resist non-equilibrium mechanical strains.[30] Additionally, the modulus also provides a measure of resilience to dendrite growth.[31] Adhesion is another property that quantifies the minimum force required to lose contact between the electrode and electrolyte (extrinsic interface). Adhesion affects the quality of electrode contact with the hybrid electrolyte and stability during cycling.[32] Increasing stress at extrinsic interfaces with higher assembly pressure results in less resistive interfaces and higher critical current densities.[33] Thus, during operation, an energy storage system can experience micromechanical stresses that can govern performance and lifetime. Techniques that can provide micro- and nanoscale spatial resolution property measurements are ideal. Raman spectroscopy is an indirect technique that can map interfaces at micron-scale resolutions and measure stress-strain relationships.[34] Raman spectroscopy is challenging for a transparent or highly reflecting material system (i.e., polymers) and also requires significant calibration and post-processing to obtain quantitative mechanical properties. Atomic force microscopy (AFM) addresses these challenges and can map mechanical properties with excellent spatial resolutions ($\approx r_{tip}$ lateral and $\leq$1 nm vertical).[35,36] AFM is a powerful tool that can probe numerous interfacial properties such as adhesion, Young's modulus, and deformation in a single scan, allowing for direct correlation with topography data that can provide valuable insight into Li ion battteries.[37–39]

In this study, we investigate how electrode|electrolyte interfacial properties (adhesion and Young's modulus) impact electrochemical performance in ASSBs with hybrid electrolytes. Extrinsic interfacial properties are systematically altered in a series of hybrid electrolytes via changing the molecular weight of the organic material (i.e., poly(ethylene oxide) [PEO]). By design, all electrolytes demonstrate similar transport properties but display varying interfacial properties. AFM is used to track the mechanical properties at the extrinsic interfaces *ex situ*. Interfacial ion transport properties are estimated using an effective mean field theory model. Variation in physical properties at the extrinsic interfaces can be correlated to the distribution of inorganic material in the hybrid electrolytes. Synchrotron X-ray nano-tomography is used to evaluate the heterogeneous distribution of inorganic particles in order to quantify the role that microstructure plays on interfacial mechanical properties. Three-dimensional (3D) structural reconstructions of hybrid solid electrolytes obtained from synchrotron experiments are combined with physics-based modeling to elucidate the origin of heterogenous interfacial properties. The findings reveal that mechanical properties at the extrinsic interface (rather than transport properties) dictate solid-state battery performance. Microstructural control over the subsurface inorganic particles within a hybrid electrolyte may enable a pathway toward controlling extrinsic interfacial properties with spatial control. This control is important for achieving facile and long-lasting Li-metal solid-state batteries.

RESULTS AND DISCUSSION

Three model hybrid solid electrolytes were processed in a ratio of 50:50 wt % between (PEO) and $Li_7La_3Zr_2O_{12}$ (LLZO) (see Supplemental Experimental Procedures). Lithium perchlorate ($LiClO_4$) is used as the salt in each polymer electrolyte. The

Table 1. Activation Energies (E_a) of Hybrid Solid Electrolyte and Polymer Solid Electrolytes

E_a (eV)	300K		1M		5M	
	$< T_m$	$> T_m$	$< T_m$	$> T_m$	$< T_m$	$> T_m$
Polymer	0.66	0.34	0.64	0.36	0.64	0.36
Hybrid	0.48	0.22	0.48	0.18	0.46	0.21

polymer molecular weight is a control variable in this study that enables a systematic approach toward altering the extrinsic interfacial properties. The molecular weight of the PEO was altered between 300,000 g mol^{-1} (300 K), 1,000,000 g mol^{-1} (1 M), and 5,000,000 g mol^{-1} (5 M). The viscosity increases with increasing molecular weight, which can impact the processing step (Figure S1B). A shear thinning behavior for 1 M and 5 M PEO is observed and suggests entangled polymer chains at a ≈4 wt % concentration in an acetonitrile solvent.

The ionic conductivity for all solid electrolytes are similar and increase from 10^{-6} S/cm at room temperature to 10^{-3} S/cm at 80°C. The electrolytes' transport properties are all similar and independent of the molecular weight of the polymer (Figure 1C). Hybrid electrolytes show improvement over the polymer electrolytes, especially at lower temperatures.[40] Hybrid electrolytes may have higher transport properties than polymer electrolytes because of a decrease in the crystallinity in the polymer matrix as well as a lower cation-polymer interaction.[11,18,40–42] Above >60°C (melting temperature of PEO [T_m]) polymer segmental motion is enhanced. At higher ceramic loading, LLZO particles can increase the tortuosity of ion transport pathways, leading to a reduction in ionic conductivity enhancement in hybrid electrolytes over the polymer electrolytes. This effect is stronger for hybrid electrolytes processed with PEO of 300 K molecular weight owing to the shorter chain lengths of these polymers.

Hybrid electrolytes show lower activation energies compared to the polymer electrolytes (Table 1). Changes in the activation energies suggest the presence of an additional ion transport pathway in the system. The intrinsic interface between the organic and inorganic phase is a potential pathway for ion conduction within these hybrid electrolytes.[6,9,11,18,43] Conductivity of these intrinsic interfaces are estimated using an effective mean field theory model. This model considers a three-component system: (1) backbone matrix (PEO), (2) filler material (LLZO), and (3) interfacial region and predicts the effective conductivity of the resultant effective medium. The following implicit equation is solved to estimate the conductivity of the intrinsic interface[44]:

$$(1-f_c)\frac{\sigma_{pol}-\sigma_{comp}}{\sigma_{comp}+Li^*\left(\sigma_{pol}-\sigma_{comp}\right)}+f_c\frac{\sigma_{int}-\sigma_{comp}}{\sigma_{comp}+Li^*\left(\sigma_{int}-\sigma_{comp}\right)}=0 \qquad \text{(Equation 1)}$$

where σ_{pol}, σ_{comp}, and σ_{int} is the conductivity of the polymer matrix, composite, and the interface, respectively; Li^* is the effective depolarization factor; and f_c is the volume fraction of the inserted grains (details in Supplemental Information).

The model estimates higher ionic conductivity for the intrinsic interfaces compared to the polymer and hybrid solid electrolytes at temperatures below the melting temperature of PEO (Figures 1D and S3). It is hypothesized that the interface could be a preferred ion transport pathway in this temperature range. Above the melting temperature, the interfacial conductivity shows a decrease for the 300 K and 1 M system. The differences in the behavior of the intrinsic interface could arise from the varying chain lengths of the polymer in these systems. Above the melting temperature, the ion transport should be favored within the polymer matrix as it shows higher ion

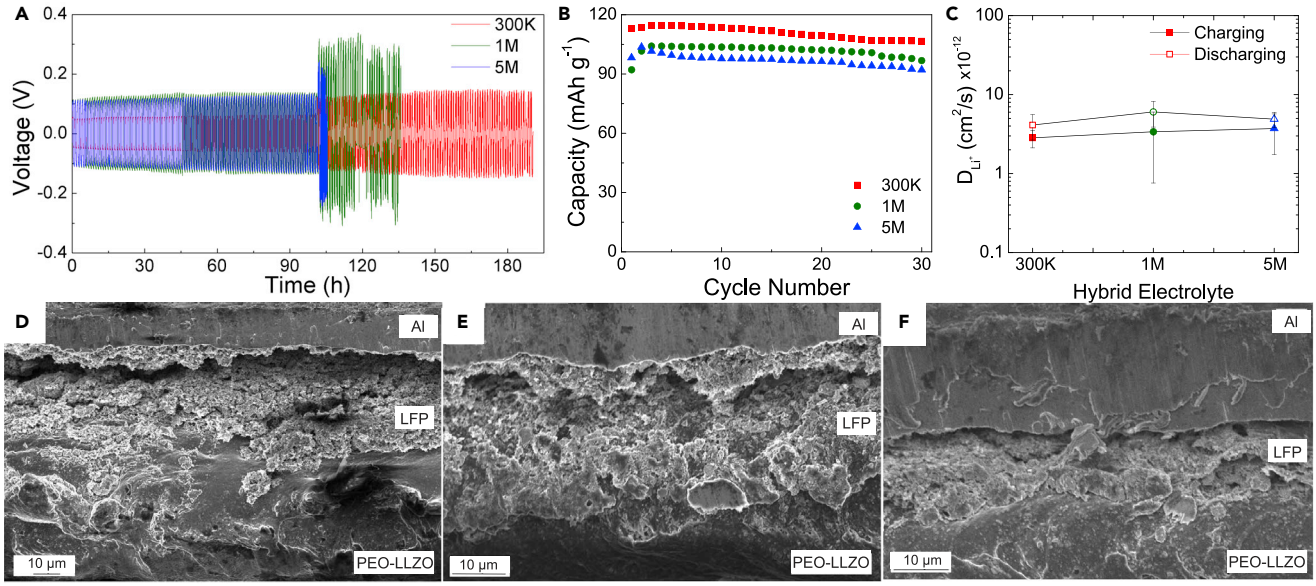

Figure 2. Electrochemical Performance of Hybrid Electrolytes and Electrode Morphology

(A) Stability tests for hybrid electrolytes in a symmetric Li|HE|Li configuration.

(B) The samples are tested at current densities of 0.2 and 0.3 mA cm^{-2}. Full-cell performance of hybrid electrolytes. LFP|HE|Li cells are assembled with 0.2 mg cm^{-2} active material loading and cycled at 0.2 C-rate.

(C) Li ion diffusion coefficients for LFP electrodes estimated from GITT.

(D–F) All electrochemical tests are performed at 60°C. SEM images of the interface of the cathode and electrolytes with 300 K (D), 1 M (E), and 5 M (F) molecular weight hybrid electrolytes (see Figures S4, S5, and S15; Table S1).

conductivity. The transference numbers for the three hybrid solid electrolytes were calculated to be 0.18 ± 0.02, 0.17 ± 0.02, and 0.18 ± 0.02 (Figure S2).

While the transport properties in each electrolyte are similar and independent of the molecular weight of the polymer, the electrochemical properties (stability and capacity) vary significantly. Hybrid solid electrolytes processed with 5 M molecular weight PEO failed significantly faster (≈100 h) than those processed with 300 K (>180 h) and 1 M molecular weight PEO (≈130 h). The charge passed to failure ($Q^{failure}$) is >2× times longer for hybrid solid electrolytes processed with 300 K than those processed with 5 M (Figure 2A; Table 2). Furthermore, full-cell experiments using a lithium iron phosphate cathode ($LiFePO_4$ or LFP) || demonstrate that the capacity and capacity retention is also dependent on the molecular weight. The 5 M hybrid solid electrolyte has the lowest capacity (92.0 mAh/g, 30th cycle) and poor capacity retention over cycle life (Figures 2B and S15). The 300 K hybrid solid electrolyte shows greater capacity retention and a significantly higher capacity (114.6 mAh/g, 30th cycle). The trends in capacity and retention for full cells and charge passed to failure ($Q^{failure}$) for symmetric cells were verified with multiple tests. Since transport properties in each solid electrolyte are similar, the variability in full-cell performance and symmetric stability testing must arise from either (1) electrode microstructure or (2) extrinsic interfacial properties.

The electrodes for all tests were processed using identical cathode inks and processing conditions. The inherent microstructure thus should be identical across the three systems. Differences, if any, should arise from the cell assembly procedure (pressure driven). Galvanostatic intermittent titration technique (GITT) and electrode imaging (scanning electron microscopy) were carried out on the three systems to quantify the effective diffusion coefficients in the electrodes. Cross-sectional scanning electron

Table 2. Electrochemical Performance Metrics of Hybrid Electrolytes
$Q^{failure}$ is calculated from Li|HE|Li cells, while retention is reported for Li|HE|LFP cells.

PEO MW (g/Mol)	$Q^{failure}$ (C)	Retention (%)
300 K	44.9 ± 1.9	92.9
1 M	25.8 ± 1.7	92.9
5 M	17.6 ± 0.7	88.8

$Q^{failure}$ is the charge passed to failure in a symmetric cell experiment. Retention is capacity retained in a full cell experiment after 30 cycles.

microscopy images demonstrate similar LFP microstructures that are independent of the electrolyte molecular weight (Figures 2D–2F and S5). Experimentally, Li diffusion coefficients can provide an indirect measure of the electrode microstructure. Tortuous ion transport pathways will lead to lower diffusion coefficients and vice-versa. The galvanostatic intermittent titration technique is used to estimate the Li diffusion coefficient for each respective cathode:

$$D_{GITT} = \frac{4}{\pi}\left[\frac{I^0 V_M}{AF}\frac{dE/dx}{dE/dt^{1/2}}\right]^2, t \ll \tau \qquad \text{(Equation 2)}$$

where I^0 (A) is the applied current, A (m^2) is the electrode area, F is the Faraday constant (96,485 C mol^{-1}), and V_M is the electrode molar volume (44.11 cm^3 mol^{-1}). Li diffusion coefficient for the three electrodes are 2.83 × 10^{-12} ± 0.71 × 10^{-12} cm^2 s^{-1}, 3.39 × 10^{-12} ± 2.63 × 10^{-12} cm^2 s^{-1}, and 3.72 × -10^{-12} ± 1.98 × -10^{-12} cm^2 s^{-1} (Figure 2C) at fully charged conditions. The diffusion coefficient is strongly dependent on the electrode microstructure (i.e., porosity and tortuosity). D^{GITT} is similar across the lithiation and delithiation range studied for the three hybrid electrolyte systems, indicating a similar microstructure. The microstructure is further evaluated by micro-tomography of the cycled electrodes (Figure S18). The porosity and tortuosity factors are quantified over a large imaged area (3 × 2 cm^2) to capture the sample heterogeneity and remove potential user bias. Pore size distributions of a 300 × 300 μm^2 sub-volume show a similar distribution across all three systems. Cycled electrodes with 300 K, 1 M, and 5 M hybrid electrolytes show an average porosity of 35%, 31%, and 33%, respectively. The tortuosity factors along the electrode thickness for the three systems are 2.13, 1.96, and 1.91, respectively. These values are consistent with the slight variation of porosity between the three systems. It is experimentally challenging to determine identical microstructures across the three samples quantitatively. However, results from the GITT measurements as well as tomography analysis suggest that the microstructures in the three systems are similar. The hybrid electrolyte films are vacuum dried overnight to remove any residual porosity in the system. Bulk electrolyte resistance measured from the 300 K, 1 M and 5 M systems are 47, 64, and 70 Ω cm^2 (at 60°C), respectively. The small difference in the bulk resistance might arise from the difference in electrolyte thicknesses between the samples. Additionally, from the definition of transference number and Nernst-Einstein equation, we know:

$$\sigma = \frac{F^2}{RT}(D_+ + D_-) \qquad \text{(Equation 3)}$$

$$t_+ = \frac{D_+}{D_+ + D_-} \qquad \text{(Equation 4)}$$

where σ is the electrolyte conductivity, F is the Faraday's constant, R is the universal gas constant, T is the absolute temperature, D^+ is the cation diffusion coefficient, D^+ is the anion diffusion coefficient, and t^+ is the cation transference number.

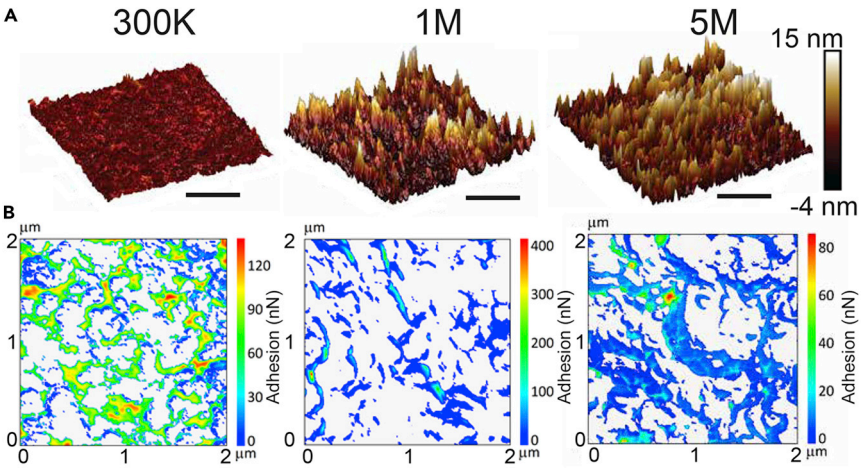

Figure 3. Atomic Force Microscopy Map of Extrinsic Interfaces

(A) 3D AFM topography images of HPEs with 300 K, 1 M, and 5 M PEO. The scale bar is 400 nm for all images and the color bar is consistent across the images.

(B) Adhesion maps for HPEs with 300 K, 1 M, and 5 M PEO. The adhesion is plotted only for regions in the scan area where the deformation is >2 nm (see Figures S6, S7, S8, and S9).

From the conductivity and transference number data for the hybrid solid electrolytes, the cation diffusion coefficient is estimated to be 5.68×10^{-10}, 2.48×10^{-10}, and 1.92×10^{-10} for the 300 K, 1 M, and 5 M system, respectively. These numbers are within the same order of magnitude, suggesting that the solid electrolyte microstructure should be similar between the three systems.

Since the electrode and solid electrolyte microstructures are similar, the electrode-|electrolyte extrinsic interfacial properties are responsible for the differences in performance (stability, capacity, and capacity retention). Extrinsic interfaces are characterized by electrochemical impedance spectroscopy (EIS) measurements of LFP|HE|Li full cells between 25°C and 75°C. The EIS spectra consist of two semicircles, followed by a tail (Figure S4). The first semicircle represents the bulk resistance (R_b) and the second semicircle collectively represents surface layer resistance (R_f) and charge-transfer impedance (R^{ct}).[45] The tail represents Warburg diffusion (W_o). The values of the resistances were calculated by using the equivalent circuit model shown in the inset of Figure S5. The 300 K hybrid electrolyte shows the lowest interfacial resistance ($4365.38 \pm 235.25\ \Omega$) at room temperature compared to the 1 M hybrid electrolyte ($5021 \pm 329.76\ \Omega$) and 5 M hybrid electrolyte ($5523 \pm 377.33\ \Omega$). Similar trends are observed between 25°C and 70°C (Table S1). Extrinsic interfacial properties govern stability, durability, and energy density. Properties that can describe an extrinsic interface are roughness, adhesion strength, and Young's modulus. AFM can simultaneously map these properties of the extrinsic interface with nanoscale resolution (Figures 3 and S17). The average roughness (R_a) is 0.57, 1.76, and 2.21 nm for the 300 K, 1 M, and 5 M hybrid electrolyte, respectively (Table 3; Figure 3A). Higher roughness for high molecular weight hybrid electrolytes suggests a higher surface energy. Smooth surfaces can enable uniform concentration gradients between the electrode and electrolyte (extrinsic interface) and are important for minimizing transport limitations and local degradation.[21]

Adhesion and Young's modulus show a heterogenous distribution over the scanned area for all the hybrid electrolytes (Figures 3B and S6). Mechanical properties are quantified only at locations where the deformation is >2 nm. The force-distance curves

Table 3. Surface Roughness of Extrinsic Interface Features for Hybrid Electrolytes Measured from AFM.

PEO MW (g/Mol)	R_q (nm)	R_a (nm)
300 K	0.74	0.57
1 M	2.33	1.76
5 M	2.80	2.21

R_g is arimethic mean roughness; R_q is root mean squared roughness.

obtained from AFM measurements are less reliable at lower deformations and hence are not used for analysis. All hybrid electrolytes show a smooth morphology (≈ 0.5–3 nm roughness) compared to their thickness (≈60 μm). The surface morphology of the hybrid solid electrolytes cannot explain the highly heterogenous distribution of the mechanical properties of the extrinsic interfaces but may be attributed to the underlying microstructure of the hybrid electrolytes. Unlike polymer solid electrolytes that are uniform at the meso scale, hybrid electrolytes can display different ceramic-aggregation properties that affect interfacial properties.

Statistical quantification of mechanical properties gives further insight into the influence of sub-surface particle distribution. All hybrid solid electrolytes show a primary adhesion peak at ≈7–10 nN (Figures 4A–4C and S7A–S7C). However, the 300 K hybrid electrolyte shows an additional peak at significantly higher adhesion values of >100 nN (Figures 4A and S7A). The 300 K hybrid solid electrolyte has a higher crystallinity, which increases the ionic salt concentration in the amorphous region. Higher salt concentrations in the amorphous region can lead to higher adhesion in these systems. The higher adhesion seen for the 300 K system can lead to better contact with the electrode at the extrinsic interface, leading to improved electrochemical performance (Figure 2). Better adhesion also prevents delamination and the loss of electrical contact during high rate charging and discharging. It should be noted that apart from the mechanical properties of the extrinsic interface, chemical properties (e.g. electrochemical window, chemical stability, and side reactions) also influence the electrochemical performance of the system.

The logarithmic distribution of Young's modulus is fitted with two Gaussian distributions (Figures 4 and S8). The peak at lower modulus is uniform and consistent across all samples, while the second modulus distribution is non-uniform. The first modulus distribution peak is 6.4, 2.8, and 3.2 GPa for 300 K, 1 M, and 5 M PEO, respectively (Figure S7A). Low molecular weight polymers (i.e., 300 K) have shorter chain lengths that can realign, entangle, or form tie molecules to transmit the stress.[46,47] The 300 K hybrid electrolytes also show a higher degree of crystallinity (Figure S1A). This results in a higher Young's modulus for the 300 K hybrid electrolyte (Figure S8A). The second modulus distribution peak shows an identical average value of 13–14 GPa for all three hybrid electrolytes (Figure S9B) with a larger distribution. The cumulative data including all the measured areas show a higher average Young's modulus for 300 K PEO (Figure S9C). Improved Young's modulus at the interface allows for better resistance against dendrite formation and thus extends the $Q^{failure}$ for the 300 K system. It should be noted that the mechanical properties reported here reflect the interaction between the AFM tip and the hybrid solid electrolyte. While the absolute value of the mechanical properties measured here will change for a composite electrode in contact with the hybrid electrolyte, the trends discussed will be consistent.

A strong correlation between the Young's modulus and adhesion is observed for all the hybrid electrolytes (Figures 4, S10, S11, and S12). The regions showing a higher Young's modulus also show relatively higher adhesion properties. This may be

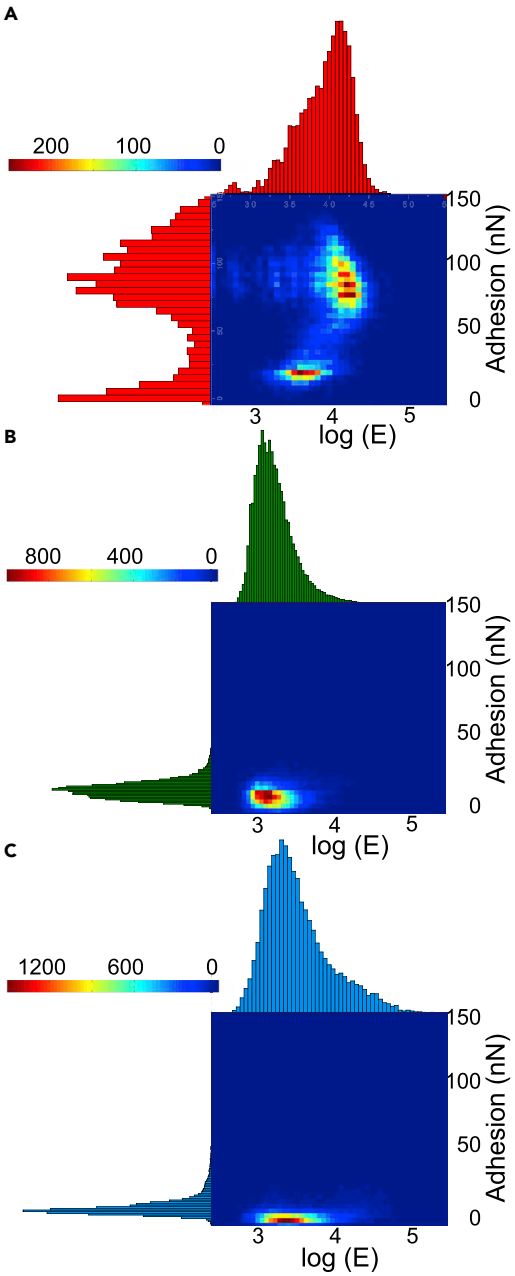

Figure 4. Quantitative Mapping of Mechanical Properties of Extrinsic Interface

(A–C) Adhesion and Young's modulus histogram and co-variance for 300 K (A), 1 M (B), and 5 M (C) hybrid electrolytes (see Figures S7, S8, S9, S10, S11, S12, and S13).

contradictory considering the mechanical properties of pristine phases separately. LLZO (150 GPa)[48] is ≈3,500× stronger than PEO (0.04 GPa).[49] Polymers show comparatively higher adhesion strength compared to ceramic particles. The strong correlation between adhesion and Young's modulus seen here cannot be described by the surface distribution of the polymer and ceramic phase. It is proposed that in hybrid solid electrolytes, the interfacial properties are greatly influenced by the composition and arrangement of the sub-surface LLZO particles. Apart from the sub-surface distribution, the ceramic particle size distribution can significantly affect

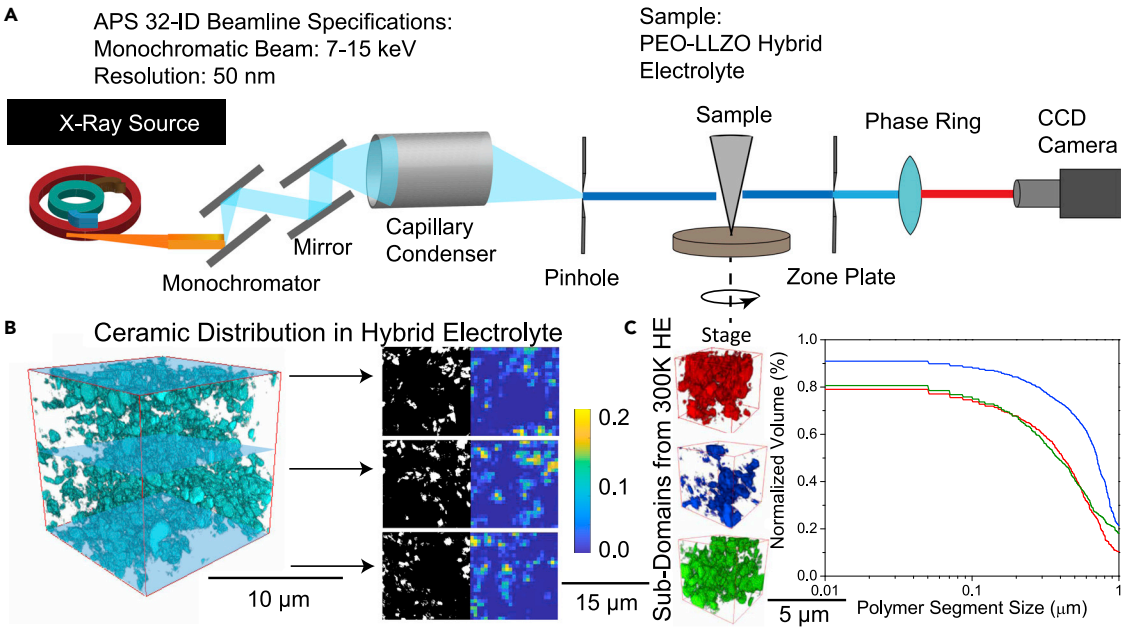

Figure 5. Synchrotron Nano-tomography Characterization

(A) Schematic diagram of the transmission X-ray microscopy technique at 32-ID beamline at Advanced Photon Source. A monochromatic X-ray source is focused through a condenser and a pinhole on the sample mounted on a rotating stage. Transmitted X-rays pass through the zone plate and phase ring on to the area detector.

(B) Representative volume showing the ceramic distribution within the hybrid electrolyte. The empty space in the sample volume depicts the polymer phase. Binarized slices at three axial positions are shown along with local polymer density at those sections. Local ceramic densities are obtained considering 500 × 500 × 500 nm^3 sub-volumes over the entire section.

(C) Representative ceramic substructures of hybrid electrolytes and the corresponding polymer size distribution.

the mechanical properties of the interface.[50] However, for this study, the LLZO particle size (≈300 nm[51]) has been kept consistent across the three samples. This was done to minimize the complexity of the sample matrix and make the deconvolution of results easier. Further work is required to evaluate the effect of particle size on the mechanical properties of the hybrid electrolytes.

It would be ideal to have a nano- or microstructure where the highly ionically conducting phase (LLZO) is uniformly distributed within the polymer phase for hybrid electrolytes. However, LLZO tends to aggregate during the processing step. The shear rates experienced during tape casting (10–100 s^{-1})[52] are not sufficient to completely break the internal structure (Figure S1B), resulting in a heterogeneous distribution of aggregated LLZO particles within the hybrid electrolytes. To further probe the origins of property heterogeneity in hybrid electrolytes, we used synchrotron X-ray nano-tomography.[53,54] This technique enables imaging of the ceramic and polymer phases within the hybrid electrolyte with nanometer-level resolutions.[51] Nano-tomography leverages attenuation contrast between the two discrete phases (polymer and ceramic) for imaging.[22] However, significant modification to the experimental optics is necessary to achieve high resolution (Figure 5A). A capillary condenser and pinhole are utilized up-beam of the sample to focus the X-rays on the sample. The transmitted X-rays are focused using a zone plate on the detector. The phase ring is added between the objective zone plate and the detector to provide additional phase contrast. Further, nano-tomography restricts the sample size to overall dimensions of <70 μm. These constraints make this technique harder to implement compared to conventional synchrotron micro-tomography. The LLZO

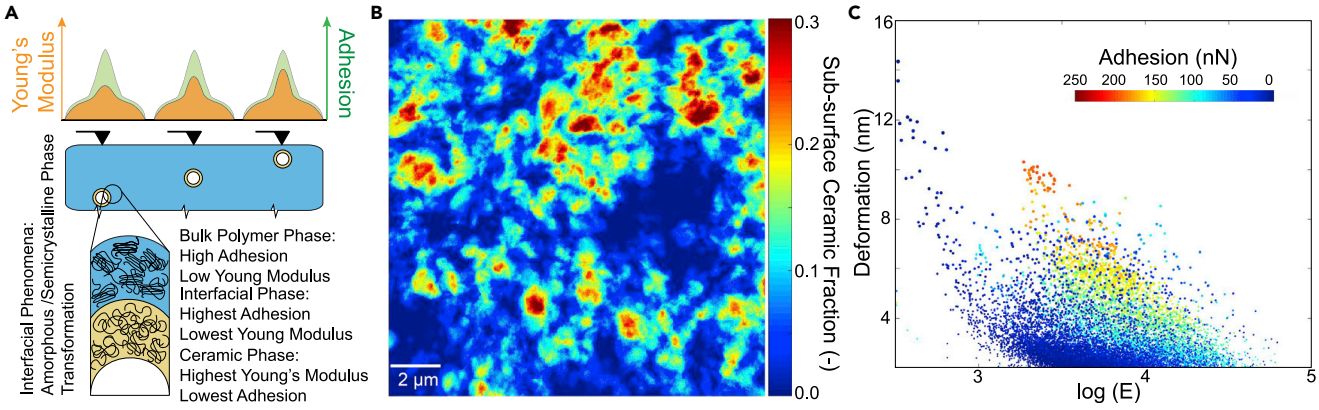

Figure 6. Sub-surface Ceramic Distribution and Impact on Mechanical Properties

(A) Schematic diagram showing the influence of the sub-structure distribution of LLZO on the mechanics of the extrinsic interfaces.

(B) Sub-surface ceramic fraction computed from the synchrotron nano-tomography dataset. Each pixel corresponds to a 50 × 50 nm spatial area. The sub-surface ceramic fraction is computed through a thickness of 20 μm. The data are for the 300 K hybrid electrolyte.

(C) Distribution of adhesion and Young's modulus for the 300 K hybrid electrolyte as a function of deformation (see Figure S14).

particles in the hybrid solid electrolytes have a characteristic size of 200–300 nm, which is within the resolution limit of this technique.

The ceramic particles within a 15 × 15 × 15 μm^3 sub-volume show a random distribution of particles. The volumetric loading of the sample (20 vol %) is close to 50 wt % samples used in the study (18.57 vol %). Binarized slices at different depths of the sample are also shown (Figure 5B). It is clearly observed that the ceramic distribution within the sample is highly heterogeneous. Local variations in ceramic density are mapped by considering 500 × 500 × 500 nm^3 sub-volumes across each slice. Even within these small domains, a large variation is seen in the local ceramic fraction varying from 0 to 0.2 within the 15 × 15 μm^2 area. Statistical studies over multiple sub-volumes show similar sizes of the polymer phase with varying distributions (Figure 5C).

The heterogenous sub-surface microstructure enables a physical interpretation of the AFM result. High Young's modulus is expected when the LLZO particles are closer to the AFM tip. This reduces the fraction of the semi-crystalline bulk polymer phase probed by the AFM tip and increases its sensitivity for the interfacial amorphous layer that possesses higher adhesion properties. It is hypothesized that the strong correlation between high Young's modulus and adhesion in the hybrid electrolytes arises because of the probing of LLZO particles close to the sample surface. This leads to a high Young's modulus value as well as the sensitivity to probe the amorphous interfacial layer that results in a high adhesion value (Figure 6A). Sub-surface variation in particle distribution can also account for the large distribution of the second Young's modulus fitting observed in the AFM data (Figure S9B). The variations in this component can arise from changing depths of LLZO particles from the AFM tip. Regions with a low or distant LLZO distribution will have lower Young's modulus than regions with a higher LLZO concentration. This is also evidenced from the co-variance of deformation and Young's modulus, which shows lower deformations reduced depth from the AFM tip increases the Young's modulus measured (Figure S13). It should be noted that the heterogenous distribution of ceramic particles arises from the agglomerate structure formation in the ink phase. The colloidal interactions between particle-polymer-solvent dictate the particle distribution and are independent of the sample casting protocols.

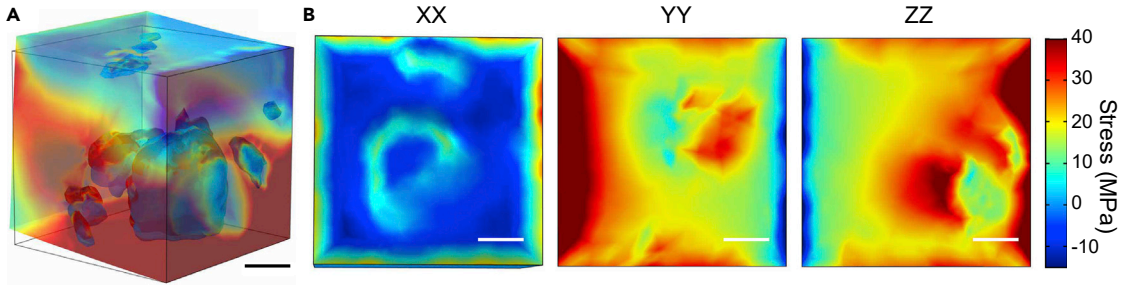

Figure 7. Mechanical Deformation Simulations

(A) Simulation results for mechanical performance of solid electrolytes. A 2 × 2 × 2 μm^3 sub-volume is extracted from the nano-tomography dataset for simulations. Stress and deformation in hybrid electrolytes subjected to 5 MPa pressure. A single surface (front right) is constrained in the simulation while load is applied on the opposite face. All other boundaries are allowed to deform freely.

(B) Principle stress distribution across the loading face along the XX, YY, and ZZ direction. All boundaries except from the loading face are considered rigid for these simulations.

The scale bar in all figures is 100 nm (see Figure S16).

Spatial variation in the sub-surface particle fraction is quantified using the nano-tomography data (Figure 6B). Each pixel in the figure represents a 50 × 50 nm area and the particle fraction are computed through a thickness of 20 μm. The particle fractions computed from the experimental ceramic microstructure show a variation between 0 and 0.3 across the imaged domain. Locations showing a lower sub-surface particle fraction are predominantly the polymer phase leading to higher deformations and correspondingly lower Young's modulus. In contrast, the locations with a higher sub-surface ceramic fraction would lead to lower deformation and higher Young's modulus. This is clearly corroborated from the AFM data (Figures 6C, S13, and S14). Adhesion also increases with an increase in deformation due to a strong correlation with Young's modulus as discussed earlier. These results reinforce the hypothesis that the sub-surface ceramic microstructure influences the mechanics of the extrinsic interfaces in the hybrid solid electrolytes.

Simulations are carried out on experimentally obtained hybrid electrolyte microstructures to provide further validation to the hypothesis. A 2 × 2 × 2 μm^3 sub-volume is cropped from the nano-tomography 3D reconstructions and imported into COMSOL (see Figure S16 for the mesh domain and boundary conditions). Young's modulus, Poisson's ratio, and density for ceramic and polymer are input into the simulation. Two simulations are carried out to investigate the influence of the heterogenous microstructure on the mechanics of the hybrid electrolyte. In the first simulation, a single surface (front right) is constrained in the simulation while a 5 MPa load is applied on the opposite face (Figure 7A). All other boundaries in the simulation are allowed to deform freely. The steady-state response of the loaded system shows a microstructure-dependent stress response. Regions containing a higher ceramic fraction in the sub-surface undergo less deformation and subsequently accrue higher (tensile) stress. In contrast, the regions containing the polymer undergo deformation and as a result show lower (compressive) stress. The free boundary condition does not replicate the AFM experiments as the hybrid electrolyte is firmly stuck on the mounting stage and the only deformable surface is the exposed, probed surface (i.e., the extrinsic interface). These conditions are replicated in another set of simulations where a similar loading is applied but with only the loading face allowed to deform while keeping the other boundaries in the system constrained (Figure 7B). The simulations were run on the same domain with loading applied to the three principle directions. The resultant stress distributions are highly heterogenous as well as directional. The sharp features at the edges are due to the

imposed constraints in the simulations. These results reaffirm the hypothesis that the ceramic microstructure within the hybrid electrolyte influence the mechanical properties of the hybrid electrolytes at the extrinsic interfaces.

Conclusions

Intrinsic and extrinsic interfaces in hybrid solid electrolytes govern ion transport, compatibility, and stability in solid-state batteries. Understanding and evaluating interfacial properties can lead to rational design of next-generation devices. Herein, we systematically study the role extrinsic interfaces (electrode|electrolyte) play on transport and performance in solid-state batteries. A series of model hybrid solid electrolytes with similar transport properties and varying interfacial properties were manufactured. Structure and property measurements indicate that extrinsic interfacial properties (rather than transport properties) largely dictate electrochemical performance. Our findings suggest that extrinsic interfacial properties can be tailored via active control. Active control over extrinsic interfacial properties can be achieved through controlled processing strategies that provide control over inorganic nano- and microstructure.

SUPPLEMENTAL INFORMATION

Supplemental Information can be found online at https://doi.org/10.1016/j.joule.2019.11.015.

ACKNOWLEDGMENTS

The authors were supported by the National Science Foundation under grant nos. 1727863 and 1847029. The authors acknowledge the Vanderbilt Institute of Nanoscience and Engineering (VINSE) for access to their shared characterization facilities. This research used resources of the Advanced Photon Source, a U.S. Department of Energy (DOE) Office of Science user facility operated for the DOE Office of Science by the Argonne National Laboratory under contract no. DE-AC02-06CH11357. AFM measurements were supported by the Fluid Interface Reactions, Structures and Transport (FIRST) Center, an Energy Frontier Research Center (EFRC) funded by the U.S. Department of Energy, Office of Science, Office of Basic Energy Sciences (W.-Y.T. and N.B.). The experiments and sample preparation in this work were performed and supported at the Center for Nanophase Materials Sciences in Oak Ridge National Lab, which is a DOE Office of Science user facility. Part of the electrochemical and materials characterization was supported by the U.S. Department of Energy, Office of Science, Basic Energy Sciences, Materials Science and Engineering Division (X.C.C.).

AUTHOR CONTRIBUTIONS

K.B.H. conceived the concept and idea. W.-Y.T. and N.B. performed the AFM measurements. M.B.D., W.Z., N.H., and V.D.A. performed the synchrotron imaging experiments. M.D. completed the image processing and analysis from the synchrotron experiments. B.H., S.V., W.Z., F.S., M.B.D., N.H., and X.C.C. helped with the electrochemical and materials characterization. M.B.D. performed all of the theoretical and modeling efforts. K.B.H. and M.B.D. wrote the manuscript.

DECLARATION OF INTERESTS

There authors declare no competing interests.

Received: September 28, 2019
Revised: October 16, 2019
Accepted: November 20, 2019
Published: January 8, 2020

REFERENCES

1. Dirican, M., Yan, C., Zhu, P., and Zhang, X. (2019). Composite solid electrolytes for all-solid-state lithium batteries. Mater. Sci. Eng. R Rep *136*, 27–46.

2. Liu, X., Li, X., Li, H., and Wu, H.B. (2018). Recent progress of hybrid solid-state electrolytes for lithium batteries. Chem. Eur. J *24*, 18293–18306.

3. Croce, F., Persi, L.L., Scrosati, B., Serraino-Fiory, F., Plichta, E., and Hendrickson, M.A. (2001). Role of the ceramic fillers in enhancing the transport properties of composite polymer electrolytes. Electrochim. Acta *46*, 2457–2461.

4. Croce, F., Appetecchi, G.B., Persi, L., and Scrosati, B. (1998). Nanocomposite polymer electrolytes for lithium batteries. Nature *394*, 456–458.

5. Kumar, B., and Scanlon, L.G. (1994). Polymer-ceramic composite electrolytes. J. Power Sources *52*, 261–268.

6. Chen, L., Li, Y., Li, S.P., Fan, L.Z., Nan, C., and Goodenough, J.B. (2018). PEO/garnet composite electrolytes for solid-state lithium batteries: from "ceramic-in-polymer" to "polymer-in-ceramic". Nano Energy *46*, 176–184.

7. Schnell, J., Günther, T., Knoche, T., Vieider, C., Köhler, L., Just, A., Keller, M., Passerini, S., and Reinhart, G. (2018). All-solid-state lithium-ion and lithium metal batteries – paving the way to large-scale production. J. Power Sources *382*, 160–175.

8. Zhang, X., Liu, T., Zhang, S., Huang, X., Xu, B., Lin, Y., Xu, B., Li, L., Nan, C.W., and Shen, Y. (2017). Synergistic coupling between $Li_{6.75}La_3Zr_{1.75}Ta_{0.25}O_{12}$ and poly(vinylidene fluoride) induces high ionic conductivity, mechanical strength, and thermal stability of solid composite electrolytes. J. Am. Chem. Soc. *139*, 13779–13785.

9. Zheng, J., and Hu, Y.-Y. (2018). New insights into the compositional dependence of Li-Ion transport in polymer-ceramic composite electrolytes. ACS Appl. Mater. Interfaces *10*, 4113–4120.

10. Keller, M., Varzi, A., and Passerini, S. (2018). Hybrid electrolytes for lithium metal batteries. J. Power Sources *392*, 206–225.

11. Zheng, J., Tang, M., and Hu, Y.-Y. (2016). Lithium ion pathway within $Li_7La_3Zr_2O_{12}$ polyethylene oxide composite electrolytes. Angew. Chem. Int. Ed. Engl *55*, 12538–12542.

12. Pandian, A.S., Chen, X.C., Chen, J., Lokitz, B.S., Ruther, R.E., Yang, G., Lou, K., Nanda, J., Delnick, F.M., and Dudney, N.J. (2018). Facile and scalable fabrication of polymer-ceramic composite electrolyte with high ceramic loadings. J. Power Sources *390*, 153–164.

13. Wang, C., Yang, Y., Liu, X., Zhong, H., Xu, H., Xu, Z., Shao, H., and Ding, F. (2017). Suppression of lithium dendrite formation by using LAGP-PEO (LiTFSI) composite solid electrolyte and lithium metal anode modified by PEO (LiTFSI) in all-solid-state lithium batteries. ACS Appl. Mater. Interfaces *9*, 13694–13702.

14. Liu, Q.Q., Petibon, R., Du, C.Y., and Dahn, J.R. (2017). Effects of electrolyte additives and solvents on unwanted lithium plating in lithium-ion cells. J. Electrochem. Soc. *164*, A1173–A1183.

15. Wang, W., Yi, E., Fici, A.J., Laine, R.M., and Kieffer, J. (2017). Lithium ion conducting poly (ethylene oxide)-based solid electrolytes containing active or passive ceramic nanoparticles. J. Phys. Chem. C *121*, 2563–2573.

16. Przyluski, J., Siekierski, M., and Wieczorek, W. (1995). Effective medium theory in studies of conductivity of composite polymeric electrolytes. Electrochim. Acta *40*, 2101–2108.

17. Yang, T., Zheng, J., Cheng, Q., Hu, Y.-Y., and Chan, C.K. (2017). Composite polymer electrolytes with $Li_7La_3Zr_2O_{12}$ garnet-type nanowires as ceramic fillers: mechanism of conductivity enhancement and role of doping and morphology. ACS Appl. Mater. Interfaces *9*, 21773–21780.

18. Zheng, J., Dang, H., Feng, Xuyong, Chien, P.-H., and Hu, Y.-Y. (2017). Li-ion transport in a representative ceramic–polymer–plasticizer composite electrolyte: $Li_7La_3Zr_2O_{12}$–polyethylene oxide–tetraethylene glycol dimethyl ether. J. Mater. Chem. A *5*, 18457–18463.

19. Ren, Y., Shen, Y., Lin, Y., and Nan, C. (2015). Direct observation of lithium dendrites Inside garnet-type lithium-ion solid electrolyte. Electrochem. Commun *57*, 27–30.

20. Rosso, M., Brissot, C., Teyssot, A., Dollé, M., Sannier, L., Tarascon, J.-M., Bouchet, R., and Lascaud, S. (2006). Dendrite short-circuit and fuse effect on Li/polymer/Li cells. Electrochim. Acta *51*, 5334–5340.

21. Dixit, M.B., Regala, M., Shen, F., Xiao, X., and Hatzell, K.B. (2018). Tortuosity effects in garnet-type $Li_7La_3Zr_2O_{12}$ solid electrolytes. ACS Appl. Mater. Interfaces *11*, 2022–2030.

22. Shen, F., Dixit, M.B., Xiao, X., and Hatzell, K.B. (2018). Effect of pore connectivity on Li dendrite propagation within LLZO electrolytes observed with synchrotron X-ray tomography. ACS Energy Lett. *3*, 1056–1061.

23. Zachman, M.J., Tu, Z., Choudhury, S., Archer, L.A., and Kourkoutis, L.F. (2018). Cryo-STEM mapping of solid–liquid interfaces and dendrites in lithium-metal batteries. Nature *560*, 345–349.

24. Wang, J.J., Guo, Z., and Xiong, S.M. (2017). Characterization of the morphology of primary silicon particles using synchrotron X-ray tomography. Mater. Charact *123*, 354–359.

25. Wang, Z., Santhanagopalan, D., Zhang, W., Wang, F., Xin, H.L., He, K., Li, J., Dudney, N., and Meng, Y.S. (2016). In situ STEM-EELS Observation of nanoscale interfacial phenomena in all-solid-state batteries. Nano Lett. *16*, 3760–3767.

26. Ohta, N., Takada, K., Sakaguchi, I., Zhang, L., Ma, R., Fukuda, K., Osada, M., and Sasaki, T. (2007). $LiNbO_3$-coated $LiCoO_2$ as cathode material for all solid-state lithium secondary batteries. Electrochem. Commun *9*, 1486–1490.

27. Takada, K., Nakano, S., Inada, T., Kajiyama, A., Sasaki, H., Kondo, S., and Watanabe, M. (2003). Compatibility of lithium ion conductive sulfide glass with carbon-lithium electrode. J. Electrochem. Soc. *150*, A274–A277.

28. Xu, L., Tang, S., Cheng, Y., Wang, K., Liang, J., Liu, C., Cao, Y.C., Wei, F., and Mai, L. (2018). Interfaces in solid-state lithium batteries. Joule *2*, 1–4.

29. Gu, M., He, Y., Zheng, J., and Wang, C. (2015). Nanoscale silicon as anode for Li-Ion batteries: the fundamentals, promises, and challenges. Nano Energy *17*, 366–383.

30. Stokes, R.J., and Fennell Evans, D. (1997). Fundamentals of Interfacial Engineering Advances in interfacial engineering series (Wiley).

31. Monroe, C., and Newman, J. (2005). The impact of elastic deformation on deposition kinetics at lithium/polymer interfaces. J. Electrochem. Soc. *152*, A396.

32. Stone, G.M., Mullin, S.A., Teran, A.A., Hallinan, D.T., Minor, A.M., Hexemer, A., and Balsara, N.P. (2012). Resolution of the modulus versus adhesion dilemma in solid polymer electrolytes for rechargeable lithium metal batteries. J. Electrochem. Soc. *159*, A222–A227.

33. Gupta, A., Kazyak, E., Craig, N., Christensen, J., Dasgupta, N.P., and Sakamoto, J. (2018). Evaluating the effects of temperature and pressure on Li/PEO-LiTFSI interfacial stability and kinetics. J. Electrochem. Soc. *165*, A2801–A2806.

34. Colomban, P. (2002). Analysis of strain and stress in ceramic, polymer and metal matrix composites by Raman spectroscopy. Adv. Eng. Mater. *4*, 535–542.

35. Griepentrog, M., Krämer, G., and Cappella, B. (2013). Comparison of nanoindentation and AFM methods for the determination of mechanical properties of polymers. Polym. Test *32*, 455–460.

36. Young, T.J., Monclus, M.A., Burnett, T.L., Broughton, W.R., Ogin, S.L., and Smith, P.A. (2011). The use of the PeakForceTM quantitative nanomechanical mapping AFM-based method for high-resolution Young's modulus measurement of polymers. Meas. Sci. Technol. *22*, 125703.

37. Huang, S., Wang, S., Hu, G., Cheong, L.-Z., and Shen, C. (2018). Modulation of solid electrolyte interphase of lithium-ion batteries by LiDFOB and LiBOB electrolyte additives. Appl. Surf. Sci. *441*, 265–271.

38. Shen, C., Hu, G., Cheong, L.-Z., Huang, S., Zhang, J.-G., and Wang, D. (2018). Direct observation of the growth of lithium dendrites on graphite anodes by operando EC-AFM. Small Methods *2*, 1700298.

39. Shen, C., Wang, S., Jin, Y., and Han, W.-Q. (2015). In situ AFM imaging of solid electrolyte interfaces on HOPG with ethylene carbonate and fluoroethylene carbonate-based electrolytes. ACS Appl. Mater. Interfaces *7*, 25441–25447.

40. Langer, F., Bardenhagen, I., Glenneberg, J., and Kun, R. (2016). Microstructure and temperature dependent lithium ion transport of ceramic-polymer composite electrolyte for solid-state lithium ion batteries based on garnet-type $Li_7La_3Zr_2O_{12}$. Solid State Ion *291*, 8–13.

41. Chen, F., Yang, D., Zha, W., Zhu, B., Zhang, Y., Li, J., Gu, Y., Shen, Q., Zhang, L., and Sadoway, D.R. (2017). Solid polymer electrolytes incorporating cubic $Li_7La_3Zr_2O_{12}$ for all-solid-state lithium rechargeable batteries. Electrochim. Acta *258*, 1106–1114.

42. Choi, J.H., Lee, C.H., Yu, J.H., Hoon Doh, C., and Lee, S.M. (2015). Enhancement of ionic conductivity of composite membranes for all-solid-state lithium rechargeable batteries incorporating tetragonal $Li_7La_3Zr_2O_{12}$ into a polyethylene oxide matrix. J. Power Sources *274*, 458–463.

43. Yang, F., Xin, L., Uzunoglu, A., Qiu, Y., Stanciu, L., Ilavsky, J., Li, W., and Xie, J. (2017). Investigation of the interaction between nafion ionomer and surface functionalized carbon black using both ultrasmall angle X-ray scattering and Cryo-TEM. ACS Appl. Mater. Interfaces *9*, 6530–6538.

44. Li, Yuanji, Zhao, Y., Cui, Y., Zou, Zheyi, Wang, D., and Shi, S. (2018). Screening polyethylene oxide-based composite polymer electrolytes via combining effective medium theory and Halpin-Tsai model. Comput. Mater. Sci. *144*, 338–344.

45. Wan, Zipei, Lei, D., Yang, W., Liu, C., Shi, K., Hao, X., Shen, L., Lv, W., Li, B., Yang, Q.H., et al. (2019). Low resistance-integrated all-solid-state battery achieved by $Li_7La_3Zr_2O_{12}$ nanowire upgrading polyethylene oxide (PEO) composite electrolyte and PEO cathode binder. Adv. Funct. Mater. *29*, 1805301.

46. Balani, K., Verma, V., Agarwal, A., and Narayan, R. (2015). Physical, thermal, and mechanical properties of polymers. In Biosurfaces: A Materials Science and Engineering Perspective, First Edition (John Wiley & Sons), pp. 1–16.

47. Landel, R.F., and Nielsen, L.E. (1993). In Mechanical Properties of Polymers and Composites. Mechanical Engineering seriesMechanical Properties of Polymers and Composites. Mechanical Engineering series (CRC Press).

48. Yu, S., Schmidt, R.D., Garcia-Mendez, R., Herbert, E., Dudney, N.J., Wolfenstine, J.B., Sakamoto, J., and Siegel, D.J. (2016). Elastic properties of the solid electrolyte $Li_7La_3Zr_2O_{12}$ (LLZO). Chem. Mater *28*, 197–206.

49. Maitra, M., Sinha, M., Mukhopadhyay, A.K., Middya, T.R., De, U., and Tarafdar, S. (2007). Ion-conductivity and Young's modulus of the polymer electrolyte PEO–ammonium perchlorate. Solid State Ionics *178*, 167–171.

50. Liu, M., Cheng, Z., Ganapathy, S., Wang, C., Haverkate, L.A., Tułodziecki, M., Unnikrishnan, S., and Wagemaker, M. (2019). Tandem interface and bulk Li-Ion transport in a hybrid solid electrolyte with microsized active filler. ACS Energy Lett. *4*, 2336–2342.

51. Zaman, W., Hortance, N., Dixit, M.B., De Andrade, V., and Hatzell, K.B. (2019). Visualizing percolation and ion transport in hybrid solid electrolytes for Li–metal batteries. J. Mater. Chem. A *7*, 23914–23921.

52. Hatzell, K.B., Dixit, M.B., Berlinger, S.A., and Weber, A.Z. (2017). Understanding inks for porous-electrode formation. J. Mater. Chem. A *5*, 20527–20533.

53. Gürsoy, D., De Carlo, F., Xiao, X., and Jacobsen, C. (2014). TomoPy: a framework for the analysis of synchrotron tomographic data. J. Synchrotron Radiat *21*, 1188–1193.

54. De Andrade, V., De Carlo, F., Gürsoy, D., Shu, D., Deriy, A., Wojcik, M.J., and Fezzaa, K. (2016). Nanoscale 3D imaging at the Advanced Photon Source. SPIE Newsroom. https://doi.org/10.1117/2.1201604.006461.